Selective CO$_2$ photoreduction to C$_2$ hydrocarbon via synergy between metastable ordered oxygen vacancies and hydrogen spillover over TiO$_2$ nanobelts

Jinbo Xue [a,b,*], Xin Jia [a,b], Zhe Sun [a,b], Huimin Li [a,b], Qianqian Shen [a,b], Xuguang Liu [a,b], Husheng Jia [a,b], Yongfa Zhu [c,**]

[a] *Key Laboratory of Interface Science and Engineering in Advanced Materials (Taiyuan University of Technology), Ministry of Education, Taiyuan 030024, PR China*
[b] *College of Materials Science and Engineering, Taiyuan University of Technology, Taiyuan 030024, PR China*
[c] *Department of Chemistry, Tsinghua University, Beijing 100084, PR China*

A B S T R A C T

The development of photocatalysts with desirable compositions and structures to improve the selectivity of CO$_2$ conversion to hydrocarbon remains a challenging goal. In this study, we present a strategy of defected TiO$_2$ nanobelts with metastable ordered oxygen vacancies by a simple Pd-catalyzed oxygen reduction method under anoxic condition. Ordered oxygen vacancies not only provide the driving force and channel for the directional movement of photoinduced electrons by modulating built-in electric field, but also promote CO$_2$ adsorption and activation. Pd nanoparticles (Pd NPs) boosted dissociation of H$_2$O to increase H* coverage and promoted the protonation of the intermediates via hydrogen spillover. The synergistic effect of ordered oxygen vacancies and hydrogen spillover contributed to the enhanced photocatalytic reduction of CO$_2$ toward C$_2$ products. The maximum selectivity of C$_2$ products can reach 51.45% with an evolution rate of 25.987 μmol·g^{-1}·h^{-1}. This strategy provides a convenient method for designing a selective CO$_2$ conversion photocatalyst.

1. Introduction

Industrialization and burning of fossil fuels, resulting in excessive carbon dioxide emissions in atmosphere, causing serious environmental issues. Semiconductor-based photocatalysis, which directly converts CO$_2$ and H$_2$O into hydrocarbon fuels and high value-added derivatives, such as CO, CH$_4$, C$_2$H$_6$ and C$_2$H$_4$, by simulating natural photosynthesis, has been recognized as a promising strategy to resolve global warming issues apart from resolving energy crises. CO$_2$ molecule consists of two linearly aligned C═O bonds with strong bond energy (750 kJ·mol^{-1}) and is therefore thermodynamically stable. This makes it difficult to be adsorbed and activated on catalyst surface [1]. Furthermore, the general form of CO$_2$ reduction to different hydrocarbons can be expressed as xCO$_2$ +y(H$^+$ +e$^-$)→C$_x$H$_{y-2}$O$_{2x-n}$ +nH$_2$O [2]. Compared to the C$_1$ products, the C$_2$ products have higher energy density and can create wider market value. The production of C$_2$ hydrocarbons requires a sufficient number of proton-electronic couplings and a sufficiently

long-lived of the adsorbed C$_1$ intermediates for C–C coupling, and the formation of C–C bonds requires overcoming larger reaction energy barrier than the formation of C–H and C–O bonds. The intricate CO$_2$ photoreduction pathways often lead to multiple possible chemicals, resulting in huge challenge for effective photoreduction of CO$_2$ into C$_2$ products. Therefore, design and development of efficient photocatalysts for CO$_2$ reduction into energy industry products is a hot topic.

Among various photocatalytic materials, one-dimensional single crystal TiO$_2$ nanobelts (TNB), an n-type semiconductor, have raised considerable attention in photocatalysis on account of their exceptional charge transport properties, special quantum confinement effect, lots of exposed active facets [3]. However, it also exist some intrinsic defects. For example, TNB are photoactive only under UV light range owing to its relatively large optical bandgap (~3.0 eV for rutile) [4]. Moreover, the low proton-electronic coupling ability of TNB lead to lower CO$_2$ reduction efficiency. These drawbacks limits substantial application of TNB.

---

* Corresponding author at: Key Laboratory of Interface Science and Engineering in Advanced Materials (Taiyuan University of Technology), Ministry of Education, Taiyuan 030024, PR China.
** Corresponding author.
E-mail addresses: xuejinbo@tyut.edu.cn (J. Xue), zhuyf@tsinghua.edu.cn (Y. Zhu).

Several strategies including band engineering, organic modification, load co-catalyst and defects formation have been applied to enhance the photocatalytic performance of TNB-based photocatalyst [5–7]. Through on-going exploration and practice, defected TiO_2 (TiO_{2-x}) with oxygen vacancies (Ov) have received growing interest in CO_2 reduction. On the one hand, introducing Ov into the lattice of TiO_2 can alter its intrinsic electronic properties and make a mid-gap below the conduction band [8], which could largely extended the light absorption range. On the other hand, recent theoretical calculations and experiments have demonstrated that surface defects on TiO_2 have shown enormous superiority in boosting the thermodynamics of CO_2 reduction reaction (CO_2 RR) by providing more capture sites for the adsorption and activation of CO_2 [9]. For example, in our previous work, black titania nanotube arrays was prepared by aluminothermic reduction for CO_2 reduction. The Ov induced new defect energy levels within the band of TiO_2 and broadened visible light absorption to improve the efficiency of CO_2 reduction [10]. Ji et al. using first-principles calculations demonstrated that the affinity between CO_2 molecule and Ov on defective surface can significantly reduce potential barrier for the deoxygenation process during photocatalytic reduction of CO_2 [11]. However, other researchers suggested that high-density crystal defects could serve as photo-generated charge carriers recombination centers, resulting in reduced photocatalytic activity [12]. Hao et al. found that the hydrogenated TiO_2 exhibited poorer photocatalytic activity compared with the pristine TiO_2 due to formation of bulk defects [13]. A number of researches have shown that Ov demonstrate enormous advantages in activating CO_2 molecules and in reducing potential barrier to CO_2 RR, but they may be detrimental to photocatalytic reactions because of the enhanced nonradiative recombination [14]. Presently, the defect distribution and function of TiO_2 are still under debate in photocatalytic process.

Notably, protons generated by dissociation of H_2O molecules on catalyst surface can migrate to the active site of adsorbed CO_2, driving the proton-electron coupling transfer processes and therefore playing an important role in the overall CO_2 RR [15]. Hydrogen spillover is a desirable pattern for dynamic migration of active hydrogen species over catalyst surface [16]. As is generally known that metal cocatalysts including Pd, Pt, Ru are beneficial for water splitting due to their special electronic structure [17]. When incorporated into the substrate, these active ingredients can accelerate water activation to increase H* coverage. These sufficient protons can attack carbon-containing intermediates, significantly enhancing the potential for further protonation of carbon-containing intermediates and thus improving the selectivity of C_2 products. In particular, introducing metal cocatalysts into the photocatalysis system not only can increase conductivity and active sites, but also accelerate charge transfer through Schottky junctions formed with semiconductors [18]. In addition, it has been reported that the incompletely occupied d–orbitals of metal cocatalyst ions have strong electrons trapping capability, which can further effectively restrain the photogenerated charge recombination and improve the properties of CO_2 conversion to C_2 products [19].

Here, following the above considerations, it is reasonable to enhance the photocatalytic CO_2 reduction capability of Ti-based oxide semiconductors through the synergistic effects of Ov and metal cocatalysts. Inspired by the above backgrounds and challenge, we prepared one-dimensional single crystal TNB with metastable Ov ordering state (Pd-Ov-TNB) via a simple Pd-catalyzed oxygen reduction method. The synthesized Pd-Ov-TNB photocatalyst has the following advantages. Firstly, one-dimensional single-crystal nanostructure has the advantages of fast electron transport and effective charge transfer. Secondly, the ordered arrangement of Ov can form a carrier-directed transport potential field, further facilitating the separation and transfer of photogenerated carriers and accelerating the adsorption and activation of CO_2 molecules [20]. Thirdly, H* generated by Pd NPs migrates to CO_2 adsorption site via hydrogen spillover to facilitate the proton-electron coupling kinetics of photocatalytic CO_2 reduction. In addition, Schottky barriers can be formed at Pd/TiO_2 interface to promote charge separation and thus enhance photoactivity [21]. Owing to the combined advantages, the synthesized Pd-Ov-TNB photocatalyst exhibits high catalytic efficiency and selectivity for conversion of CO_2 to C_2 products under mild conditions.

2. Experimental section

2.1. Synthesis of palladium nanoparticles (Pd NPs)

As described elsewhere [22], in a typical synthesis of Pd NPs, 8 mL of an aqueous solution containing PVP (105 mg), ascorbic acid (60 mg), and potassium bromide (500 mg) were placed in a 25 mL beaker and heated at 80 °C preheat under magnetic stirring for 10 min. Then, 3.0 mL of an aqueous solution containing Na_2PdCl_4 (57 mg) was added into the reaction flask, and the reaction was allowed to proceed for 3 h. The product was collected by centrifugation and washed several times with ethanol to remove excess PVP. Finally, the product was dispersed in 7.5 mL of ethanol to form a suspension at a concentration of 2.74 mg·mL^{-1}.

2.2. Catalyst preparation

TNB films were fabricated using Pd-catalyzed oxidation method. As shown in Fig. 1, TiO_2 sol was prepared according to our previous work [23]. Then, TiO_2 sol layer was uniformly deposited on pure titanium foils (99.95%) using a homogeniser (KW-4A), and annealed at 300 °C in air for 30 min with a heating rate of 3 °C·min^{-1} to form a thin continuous oxide film on Ti surface. Secondly, 0.2 mL Pd NPs suspension was drop-coated on the surface of TiO_2 sol layer using a spin coating method with rotation speed at 100 r·min^{-1} for 15 min until Pd NPs were uniformly distributed. Finally, the samples were placed horizontally in an alumina crucible and annealed at 800 °C in argon for 4 h with a heating rate of 3 °C·min^{-1}. TNB arrays with metastable ordered Ov could be prepared using this process, denoted as Pd-Ov-TNB. The compared samples were also prepared using a similar method for exploring the formation mechanism and performance test. Pd-Ov-TNB were immersed in concentrated nitric acid for 1 h to remove the Pd NPs. Subsequently, the products were washed thoroughly with deionized water and dried at 50 °C for 12 h, denoted as Ov-TNB. While Pd-Ov-TNB were further annealed at 400 °C in air for 2 h to repair Ov, denoted as Pd-TNB.

2.3. Characterization

The morphologies of catalysts were investigated using field emission scanning electron microscopy (FESEM; JEOL JSM-6700 F, Japan) and high resolution transmission electron microscopy (HRTEM; JEOL JEM-2100 F, Japan). The phase and lattice parameters of catalysts were characterized by X-ray diffraction (XRD; SmartLab, Rigaku), with diffraction patterns were collected with a 2° step size between 20° and 80° (2θ). The surface element state of catalysts were measured by X-ray photoelectron spectroscopy (XPS; Thermo Fisher ESCALAB 250XI, USA). The Ov concentration of photocatalasts were detected by electron paramagnetic resonance (EPR; Bruker E500, Germany) at g= 2.001. Photoluminescence measurements were obtained on a Shimadzu RF-5301PC spectrometer (PL/TRPL; Edinburgh FLS980, UK). Ultraviolet-visible diffuse reflectance spectroscopy (UV–vis DRS; PerkinElmer Lambda 950, USA) was used to analyze light absorption of catalysts using $BaSO_4$ film as reference material, and the wavelength scanning range was 250–800 nm. Photogenerated charge carrier behaviors were analyzed by surface photovoltage (SPV), measured in a wavelength range from 250 to 800 nm (CHF-XM500W, PerfectLight, China).

2.4. Photoelectrochemical experiment

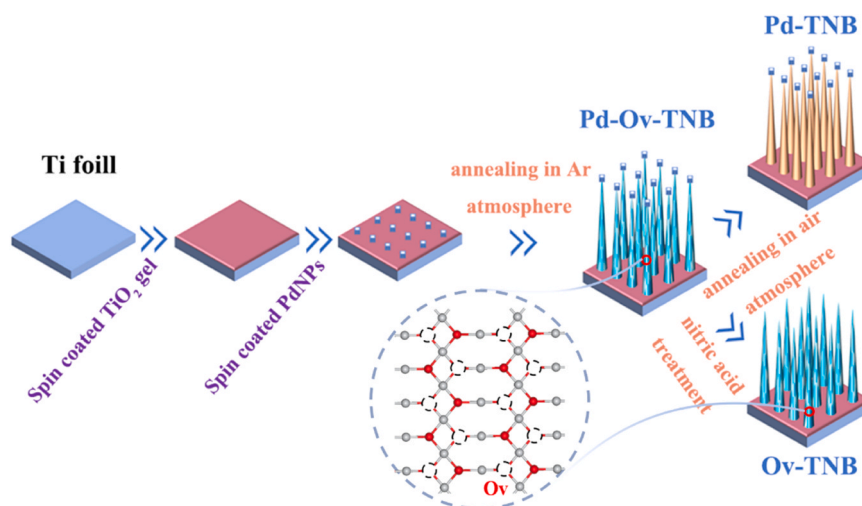All electrochemical tests were carried out using a three-electrode

Fig. 1. Schematic illustration for synthesis of Pd-Ov-TNB, Pd-TNB and Ov-TNB.

system on an electrochemical workstation (AUTOLAB-PGSTAT30) with 1 M NaOH solution as the electrolyte. In the experiment, the prepared catalyst, Pt sheet and saturated calomel electrode (SCE) were used as working electrode, counter electrode and reference electrode, respectively. Transient photocurrent time measurements were performed using a 300 W xenon lamp as the light source. Mott−Schottky (M−S) analyses were measured at a frequency of 1 kHz with perturbation signal of 5 mV. Electrochemical impedance spectroscopy (EIS) was conducted at open-circuit voltage in the frequency range of 0.1–100 kHZ.

2.5. Evaluation of photocatalytic activity

The photocatalytic test was performed in a high-pressure visible photocatalytic reactor (WCGF-25, Xi'an Taikang Bio-logical Technology, China). A 300 W xenon lamp was utilized to create simulated solar illumination intensity of 300 mW·cm^{-2} under AM 1.5 G filter. The specific process was as followed: the sample was placed on the top of reactor, and 2 mL of deionized water was injected into the reactor as electron donor. Before irradiation, the reactor was purged with high purity Ar (99.999%) for 30 min to remove air. After that, 50 mL of high-purity CO_2 was introduced into the reactor, and then the reactor was closed. After 5 h of sealed light exposure, a gas chromatograph (Agilent 8890, USA) equipped with a flame ionization detector (FID) was used to detect the gaseous products after CO_2 reduction.

2.6. In-situ DRIFT measurements

In situ diffuse reflectance infrared Fourier transform spectra (DRIFTS) testing was performed with Bruke Tensor II FTIR spectrometer (In-situ DRIFT, Bruker TENSOR II, Germany). The samples were first sealed in the specimen chamber and purged with Ar for 30 min to remove impurities. After that, a continuous mixture of CO_2 and H_2O was introduced and infrared absorption spectra were recorded. And then, the full spectrum light (CHF-XM300W, PerfectLight) were introduced to irradiate, FTIR spectra were collected over time.

2.7. Theoretical calculations

All theoretical calculations were performed using the CASTEP module of Materials Studio. We constructed $2 \times 2 \times 3$ supercells of rutile TiO_2 and set Ov at different positions. The structural relaxations were performed until the force of atom convergence is 0.01 eV/Å. In energy calculations, the K-point grid was set to $2 \times 2 \times 2$, and the maximal displacement value was set to 5×10^{-4} Å.

3. Results and discussion

3.1. Construction catalyst with ordered oxygen defect by Pd-catalyzed oxygen reduction method

The morphologies of as-prepared samples were characterized by FESEM. As shown in Fig. 2a, the length of Pd-Ov-TNB is approximately 4–8 μm, with widths of 100–300 nm and 10–20 nm at the bottom and tip, respectively. It should be noted that there exists a Pd seed at the tip of each nanobelts, as marked by dashed circles in Fig. 2a, and energy dispersive X-ray spectroscopy (EDS) results show that the seeds are Pd NPs (Fig. S1). In addition, an obvious layered structure can be observed from cross-sectional SEM image of Pd-Ov-TNB, as shown in Fig. 2b. As seen from EDS line scans on cross-sectional image (Fig. S2), the layered structure can be identified as pre-oxidized layer, TiO_2 columnar crystal, and nanobelt layer from bottom to top, respectively (Fig. 2b). Compared with Pd-Ov-TNB, Pd NPs at the tip of Ov-TNB are disappeared (Fig. S3a), and EDS results only showed characteristic peaks of Ti and O elements (Fig. S4), indicating Pd NPs are successfully removed from this sample. It is also noteworthy that there is no obvious difference in morphology between Pd-TNB and Pd-Ov-TNB (Fig. S3b), indicating that secondary heat treatment process had no significant effect on TiO_2 nanobelts morphology.

Fig. 2c showed XRD patterns of all samples. All diffraction peaks fit the typical rutile standard card (PDF No. 75–1748). Minor diffraction peaks of Ti is also observed due to Ti substrate. Even for the samples containing Pd NPs, no characteristic peaks attributable to Pd or Pd oxides are observed, which can be attributed to the high dispersion or low content of Pd species. However, the ionic radius of Pd ion (0.085 nm) is larger than that of lattice titanium ion (0.068 nm) [24]. Therefore, it is difficult for Pd to enter TiO_2 crystals lattice, but exists as nanoparticles. Compared with Pd-Ov-TNB and Ov-TNB, the sharp reflection peak of Pd-TNB may be attributed to enhanced crystallinity of secondary annealing. It is generally accepted that in XRD analysis, the intensity of diffraction peaks is related to crystallinity of the samples, Pd-Ov-TNB and Ov-TNB exhibits lower diffraction peak intensity, implying that the introduction of Ov may disturb the periodicity of crystal structure.

Further, electron paramagnetic resonance (EPR) measurements were employed to demonstrate the defect states of different samples. As show in Fig. 2d, Pd-Ov-TNB exhibits an intensive EPR signal at $g = 2.001$, which may be attributed to the existence of Ov [25]. The EPR signal of Ov-TNB sample is stronger than that of Pd-Ov-TNB, indicating that the removal of Pd NPs inevitably lead to formation of new structural defects on surface of TiO_2 nanobelts, resulting in a higher concentration of Ov in Ov-TNB. Moreover, no EPR signal is detected in Pd-TNB, indicating that
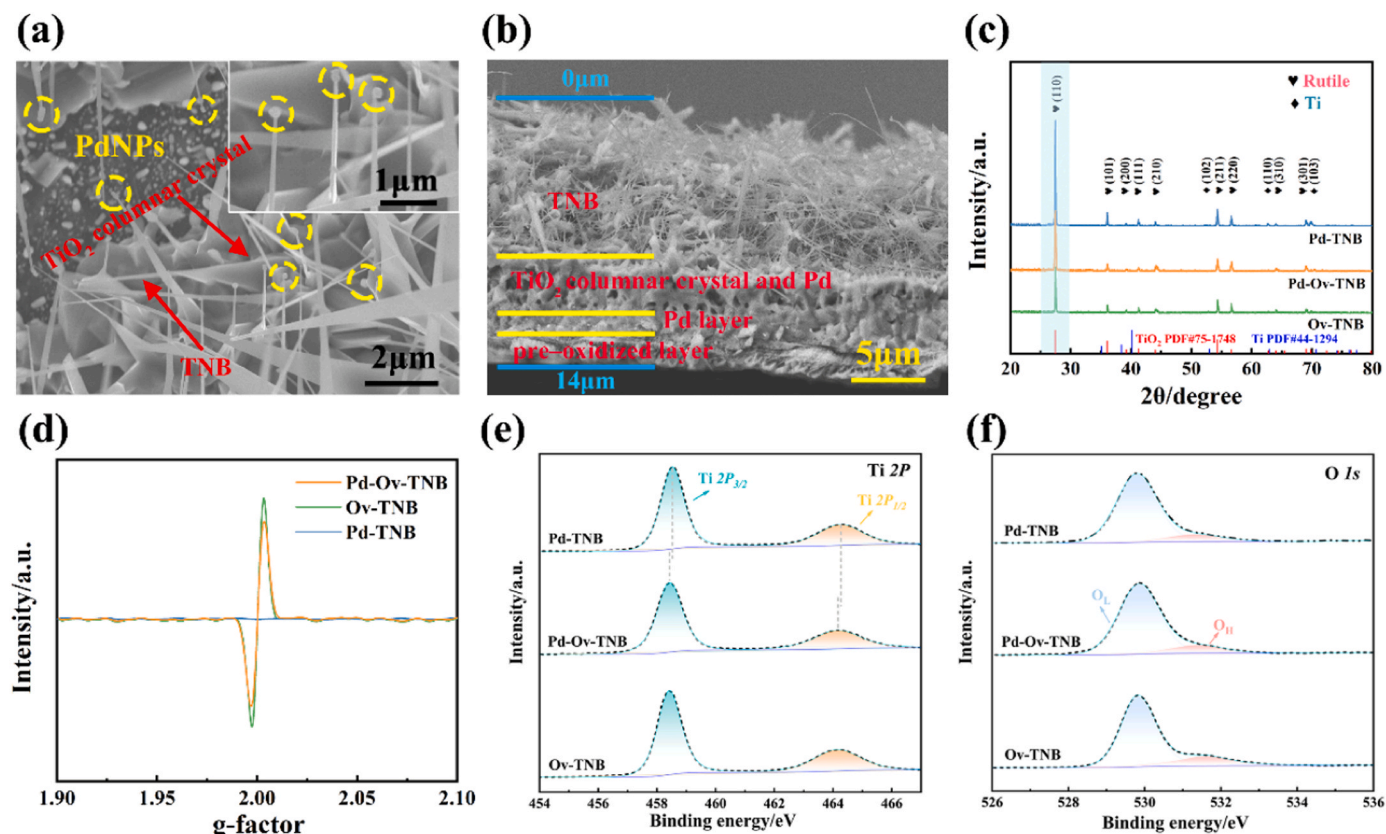
Fig. 2. Micromorphology and Chemical environment analysis of three catalysts. SEM images of (a) Pd-Ov-TNB and (b) cross-sectional image of Pd-Ov-TNB; (c) XRD patterns; (d) EPR spectra; (e) high-resolution XPS spectra of Ti 2p, (f) O 1 s.

the Ov on Pd-Ov-TNB are repaired by secondary annealing in air. Generally, The Ov sites can be used as electron sinks, which effectively facilitating the adsorption and activation of CO_2 molecules, thereby promoting CO_2 RR.

The chemical state and bonding configuration of photocatalysts were further characterized by X-ray photoelectron spectroscopy (XPS) analysis. Fig. 2e and f show XPS peaks of Ti 2p and O 1 s of all samples. For Ti 2p profile, the binding energies at 464.2 and 458.5 eV correspond to Ti^{4+} ($2p_{1/2}$ and $2p_{3/2}$) [26]. For Pd-Ov-TNB and Ov-TNB, the peaks of Ti 2p are slightly shifted towards lower binding energy, which can be attributed to the introduction of Ov [27], as shown in Fig. 2e. Fig. 2f shows the high-resolution O1s XPS spectra with the binding energies at 529.7 and 531.8 eV correspond to Ti-O-Ti surface lattice oxygen (denoted as O_L) and Ti-OH surface hydroxyl (denoted as O_H), respectively [28]. In general, a defective oxygen site may bind to a hydrogen atom and locally form a surface hydroxyl group, and the relative intensity of Ti-OH peak of TiO_2 is a main criterion to judge the presence of Ov [29]. The peak area of oxygen deficiency in Pd-Ov-TNB and Ov-TNB photocatalysts are larger than in Pd-TNB, indicating the presence of Ov in as-synthesized photocatalysts, which may favor the activation of CO_2 [30]. The ratio of peak areas of O_H to ($O_L + O_H$) (%) is listed in Table S1. To further analyze formation mechanism of TNB, Pd 3d XPS spectra of all samples are recorded in Fig. S5. For Pd-Ov-TNB and Pd-TNB photocatalysts, the binding energies at 336.8 and 342.2 eV are corresponding to the characteristic peaks of Pd $3d_{5/2}$ and $3d_{3/2}$ for metallic Pd, the observed peaks at 337.8 and 343.3 eV are assigned to Pd $3d_{5/2}$ and $3d_{3/2}$ of PdO [31], which matches well with preparation process of TNB. During annealing process, the surface layer of Pd NPs decompose O_2 to O^{2-} for formation of PdO. According to Ellingham diagram (Fig. S6), the formation energy of Ti oxide (TiO_2) is lower than that of PdO, so PdO reacts with Ti^{4+} diffused from the substrate at high temperature to form Pd and TiO_2, and eventually Pd exists in the form of the metallic state

and PdO. In contrast, no peaks corresponding to Pd species are observed in Ov-TNB.

Transmission electron microcopy (TEM) observations were performed to provide more detailed information of as-prepared Pd-Ov-TNB sample. The nanobelt with length of 1.4 μm and diameter of 25 nm is observed in Fig. 3a, which is consistent with SEM results. Coarse and irregularly shaped nanoparticles are also observed at the tip of nanobelt due to agglomeration of Pd NPs by dewetting effect during high temperature annealing treatment [32], and clear lattice stripes corresponding to cubic Pd(111) planes are observed in Fig. S7a. The lattice spacing of 0.33 nm and 0.29 nm correspond to rutile TiO_2 (110) and (001) crystal planes well, as shown in Fig. 3b. The selected area electron diffraction (SAED) patterns reveal a set of spots corresponding to (110), (001) and (111) planes of rutile phase, as shown in Fig. 3d. Both HRTEM image and diffraction patterns demonstrate that TNB have a single-crystal structure with [001] growth direction. Meanwhile, a clear modulated structure are shown in the enlarged HRTEM image, as shown by the red line in Fig. 3c. The production of the modulated structure indicates the possible presence of a superstructure in our prepared material. To further confirm the cause of the modulated structure, CrystalMaker software was used to construct the corresponding rutile TiO_2 crystals (Fig. 3e) and the diffraction pattern of these TiO_2 crystals were simulated by SingleCrystal software (Fig. 3f). Interestingly, the diffraction spots of perfect crystal are periodically missing compared to SAED pattern in Fig. 3d, as shown by the dashed circles in Fig. 3f. The extra spots in SAED patterns of Pd-Ov-TNB suggested a possible superstructure. This superstructure is suggested to be caused by the ordering of Ov inside TNB during growth. Similar results were also found in previous reports and other materials [33–35]. As Wang's reported, Ov ordering occurrs in (110) plane, forming a zigzag chain along [001] direction in rutile TiO_2 crystals [33]. The corresponding oxygen atoms are removed from rutile TiO_2 crystal, as shown in Fig. 3g. The diffraction pattern of
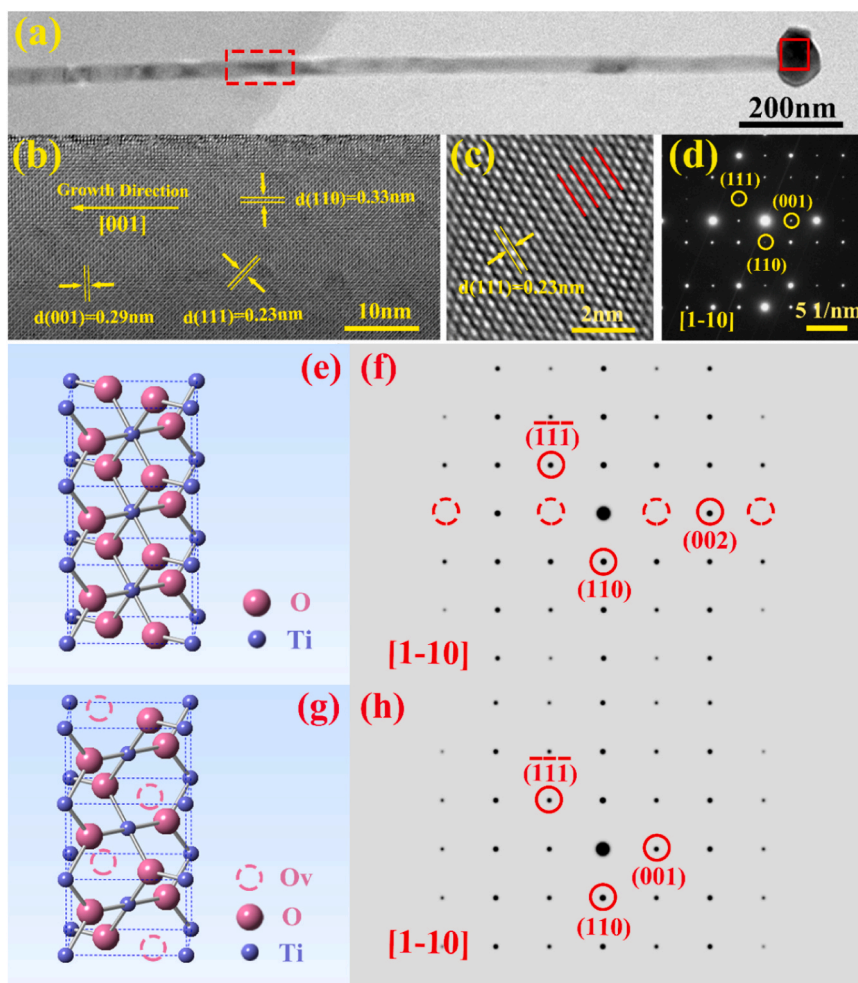
Fig. 3. Microscopic characterization of Pd-Ov-TNB. (a) TEM image, (b) typical HRTEM image, (c) enlarged HRTEM image and (d) SAED pattern of Pd-Ov-TNB; corresponding structural simulation analysis: (e) perfect TiO$_2$ crystal and (g) TiO$_2$ crystal with ordered Ov; (f, h) the corresponding SAED patterns.

this defective crystal is simulated again using SingleCrystal software, and the diffraction spots recovered to the experimental level, as shown in Fig. 3h. This confirmed that the additional diffraction spots are caused by the ordering of Ov.

The mechanism of formation of ordered Ov on the (110) crystal plane was further investigated by first-principles density functional theory (DFT) calculations, as shown in Fig. 4. Based on the formula $E_f = E_d - E_p - 3/2E_o$ (where d represents we constructed TiO$_2$ cell with Ov defective, p indicates TiO$_2$ without Ov defects, and O stands for oxygen), we calculated the formation energy along the 001 direction deducting the different Ov, and presented the results in the Table S2. It can be
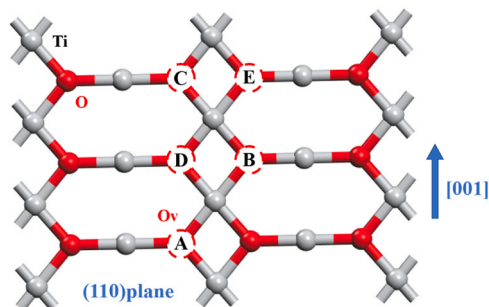

Fig. 4. Different arrangements of oxygen vacancies on the (110) crystal plane along the [001] direction.

observed that the lowest formation energy is 20.2052 eV when the Ov is arranged in a ABC zigzag arrangement. Therefore, Ov tend to be arranged in this pattern.

In order to clearly investigate growth details of nanobelts with ordered Ov, the possible growth processes based on the discussion of above experimental results were shown in Fig. 5. In the general view of metal oxidation [36], metal cations reaction with oxygen anions to form an oxide layer by diffusion effect at high temperature. When the oxygen partial pressure is sufficiently high, the oxidation process is controlled by diffusion. However, when the oxygen partial pressure is sufficiently low, the process will be interface reaction rate controlled by the oxygen reduction reaction [37]. In this work, the oxygen reduction catalyst confines the reaction and drives nanobelts growth as the entire annealing process in an oxygen-deficient environment. The Pd NPs are uniformly spin-coated on the pre-oxidised Ti foil. According to Ellingham diagram (Fig. S6), the Gibbs free energy for formation of Ti oxide (TiO$_2$) is lower than that of PdO, so PdO reacts with Ti^{4+} diffused from the substrate at high temperature to form Pd and TiO$_2$, as noted in (Eq. (1)).

$$Ti^{4+} + PdO + O^{2-} \rightarrow TiO_2 + Pd \tag{1}$$

During annealing, Ti^{4+} diffuses rapidly and pre-set Pd NPs can be used as nucleating agents to stimulate the rapid growth of TiO$_2$ crystals, forming a columnar crystal layer with a thickness of about 3 μm. At the same time, some of Pd NPs are wrapped in TiO$_2$ grains, thus losing their role in catalyzing oxygen decomposition, while another small fraction
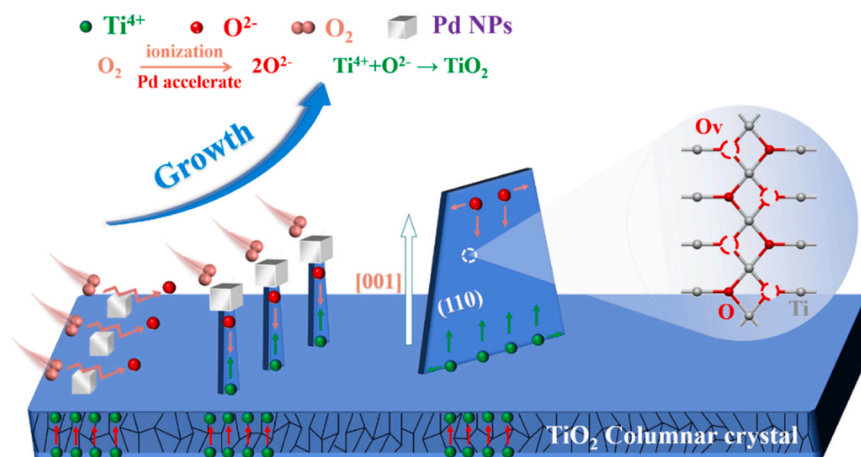
Fig. 5. Schematic of the growth process for TNB containing ordered Ov.

are retained on the surface of TiO$_2$ columnar crystals. At this point, rapid oxygen exchange at Pd NPs surface confined the reaction (Eq. (1)), which promotes TiO$_2$ nanobelts unidirectional growth under Pd NPs guidance [38]. Due to the whole process takes place in an anoxic environment, Ov are introduced into TNB during the early stage of nanobelts formation.

As previous researches, Gu et el. reported an unexpected LaCoO$_{2.5}$ phase with a zigzag-like oxygen vacancy ordering through annealing a compressive-strained LaCoO$_3$ in vacuum [39]. Aschauer et al. also found that strain differentiates modulates Ov ordering in CaMnO$_3$ film [40]. This presumes that the lattice strain significantly lowers the ordering oxygen vacancy formation energy in oxide materials. In our work, the lattice distortions between TiO$_2$ columnar crystals and TNB induces the internal strain, which is helpful for accumulation and aggregation of Ov with a certain periodicity. The degree of strain of a material can be inferred from XRD-related information. The strain present within the sample is analysed using the Halder-Wagner (H–W) plot [41], and the formula is as follows

$$\left(\frac{\beta}{\tan\theta}\right)^2 = \frac{K\lambda}{D_{HW}} \bullet \frac{\beta}{\tan\theta\sin\theta} + 16\varepsilon_{HW}^2 \quad (2)$$

where ε_{HW} and D_{HW} denote the strain and crystallite size of the TNB films, respectively; K = 0.9 is the shape factor; β, λ, and θ represent the FWHM, the wavelength of Cu Kα radiation, and the X-ray diffraction angle, respectively. From the calculations and the H–W plot (Fig. S8), it can be found that the most obvious strain in Pd-Ov-TNB may be induced by the lattice mismatch between the TiO$_2$ columnar crystals and the TNB, and consequently contribute to the generation of ordered Ov. The significant reduction of strain after secondary annealing confirms that internal strain in material is a key factor in the generation of ordered Ov. Sufficiently high concentration of Ov are thermally activated at high temperatures, increasing its mobility and favouring the ordering state of Ov [42].

So far, the modulated structure of ordering Ov is formed in the initially growth of TiO$_2$ nanobelts. The continuous growth of ordering Ov is associated with the transportation of O^{2-}. Due to serious oxygen deficiency in nanobelts, O^{2-} is aggregated near Pd NPs. Then, under the effect of the chemical potential gradient, O^{2-} enriched in Pd NPs region diffuses randomly in the nanobelts. However, the migration of O^{2-} along the ordering Ov is accelerated, which is much quicker than the diffusion in other directions. Through continuous growth in annealing, a one-dimensional nanobelts structure is formed. Since the production rate of O^{2-} and the growth rate of the nanobelts are balanced, the ordered Ov are retained in the oxygen-deficient atmosphere.

3.2. Synergistic effect between ordered Ov defect and Pd NPs improved photoinduced charge transfer

In order to evaluate the optical absorption properties of photocatalysts, UV–vis diffuse reflectance spectra (DRS) of all samples were investigated, as shown in Fig. 6a. A steep absorption edge at ∼410 nm can be observed, which belongs to the intrinsic band-band transition of rutile TiO$_2$, corresponding to gap of 3.05 eV. Based on these spectra , the band gap energy (eV) of all samples was calculated using Tauc equation, as shown in Fig. S9a. The energy band gap (E_g) of Pd-Ov-TNB, Ov-TNB, and Pd-TNB were estimated to be 3.06, 3.06 and 3.11 eV respectively. The optical absorption edge of Pd-Ov-TNB and Ov-TNB apparent redshift, indicating that the introduction of ordered Ov have an effect on the energy band structure of TNB and the optical absorption range are effectively widened. The stronger incident light absorption was beneficial to production of more photoinduced carriers [43].

PL emission spectra of samples were conducted to investigate the migration and recombination efficiency of photogenerated carriers, as shown in Fig. 6b. All samples exhibited PL signals with similar curve shapes. All samples display strong emission peaks in 350–500 nm wavelength range with the excited wavelength of 250 nm. The spectral peak at 470 nm corresponds to the intrinsic defect energy level of TiO$_2$ [44]. The emission intensity of Pd-TNB is obviously reduced compared with Ov-TNB, indicating that Pd NPs can inhibit photogenerated carrier recombination by trapping photogenerated electrons. The weakest emission intensity is also observed for Pd-Ov-TNB, which is due to the fact that Ov can act as charge traps, increasing the electron concentration and hindering the recombination of electrons and holes [45]. In addition, metastable ordered Ov act as carrier separation and transport channels, facilitating the migration of free electrons to the surface. Ordered Ov and Pd NPs could synergistically promote further separation of photogenerated charges. These advantages would enhance the photocatalytic CO$_2$ reduction performance of Pd-Ov-TNB photocatalyst.

Surface photovoltage spectroscopy (SPV) technique was conducted to further investigate the behavioral mechanism of photogenerated charge transfer at the material interface by revealing the kinetic behaviors of photogenerated charge carriers [46]. SPV amplitude spectra of all samples were shown in Fig. 6c. The positive photovoltaic signal of samples also conforms to the characteristics of n-type semiconductor. It should be noted that Pd-Ov-TNB shows the highest SPV response. Based on the above fact, it is hypothesized that the presence of ordered Ov and Pd NPs play a positive role in charge separation, and the results are consistent with PL results. Importantly, SPV response range of Pd-Ov-TNB and Ov-TNB are significantly broadened, indicating that the presence of ordered Ov can enhance visible-light absorption and possess effective separation of photogenerated charges. The above results
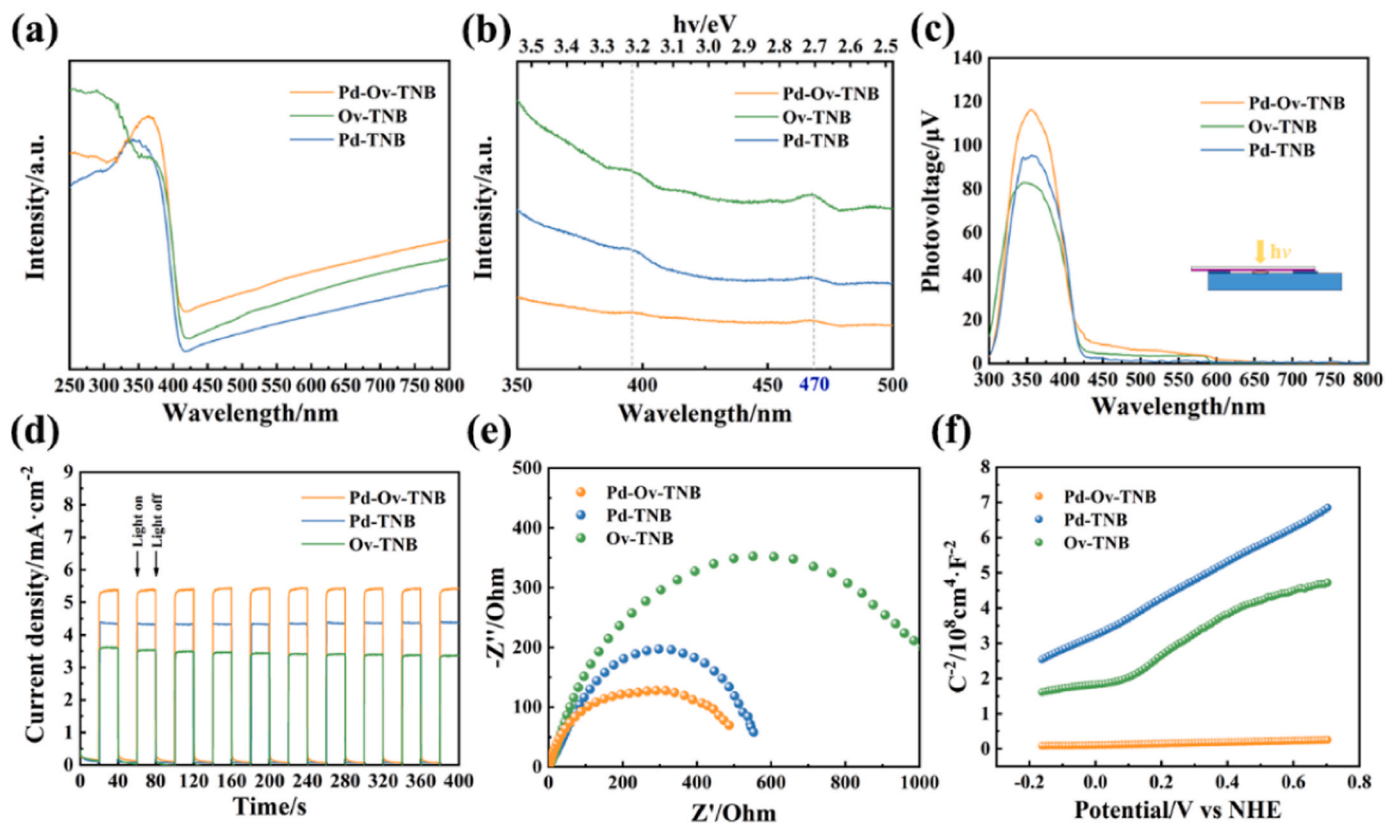
Fig. 6. Light absorption and carrier behavior evaluation of Pd-Ov-TNB, Ov-TNB and Pd-TNB. (a) UV–vis absorption spectra; (b) PL emission spectra; (c) SPV spectra; (d) transient photocurrent responses; (e) EIS plots and (f) Mott−Schottky plots.

indicate that the modulated structure of Pd NPs and ordered Ov drive photogenerated electrons to the catalyst surface, facilitating the surface reaction.

In addition, a series of photoelectrochemical tests were carried out to explored the photogenerated carrier transfer efficiency. All samples exhibited reversible photocurrent response, as shown in Fig. 6d. The order of photocurrent intensity is Pd-Ov-TNB > Pd-TNB > Ov-TNB. Pd-Ov-TNB exhibited the strongest photoresponse under illumination (5.38 mA·cm^{-2}). Higher current intensity indicates higher electron-hole separation efficiency. This demonstrates that Pd species and ordered Ov as well as one-dimensional morphology can effectively promote the separation of carriers. Electrochemical impedance spectroscopy (EIS) was further performed to make out the surface charge transfer of samples, as shown in Fig. 6e. Nyquist plots of different photocatalysts show similar shapes, with the diameter of semicircle representing the charge transfer resistance. The smallest semicircular Nyquist plot for Pd-Ov-TNB indicates efficient photogenerated charge transport.

Further, Mott−Schottky (M−S) plots were obtained under full-spectrum irradiation for investigating the carrier charge concentration of semiconductor materials, as shown in Fig. 6f. All curves show a positive slope, which is a property of n-type semiconductors. The pho-togenerated carrier concentration of all samples can be calculated using the following formula:

$$N_d = \frac{2}{e\varepsilon_0\varepsilon}\frac{d(E - E_{fb} - KT/e)}{d(1/C^2)} \qquad (3)$$

Where e, ε, ε_0, and $d(E\text{-}E_{fb}\text{-}KT/e)$ represent the electron charge, dielectric constant of rutile TiO_2 (170 for rutile) [47], vacuum dielectric constant and the inverse of the slope of M−S curve, respectively. The carrier densities of these samples are 2.09×10^{20} cm^{-3} for Pd-Ov-TNB, 1.51×10^{18} cm^{-3} for Pd-TNB and 1.31×10^{18} cm^{-3} for Ov-TNB. Higher carrier concentration indicates effective charge transfer of samples

under light irradiation.

In general, the overall photoelectrochemical properties of the TNB are always related to their photocatalytic performance. The built-in electric field constructed by ordered Ov provides a channel for the directional transmission of photogenerated carriers, which enhances the separation and transport of photogenerated carriers. At the same time, the Schottky barriers constructed by Pd/TiO_2 interface further facilitates the separation of photogenerated carriers. Consequently, the modulated structure of Pd NPs and ordered Ov drives photogenerated charge migration to the catalyst surface, providing an electron-rich environ-ment for photocatalytic CO_2 reduction. Thus, the synergistic interaction of Pd NPs and ordered Ov will enhance the efficiency of photocatalytic CO_2 reduction.

3.3. Synergistic effect between hydrogen spillover and ordered Ov defect enhanced yield and selectivity of C_2 hydrocarbon

The obtained samples were used as photocatalysts for CO_2 reduction, and the photocatalytic reduction of CO_2 with water vapor was con-ducted under full-spectrum irradiation for 5 h and at atmospheric pressure. The photocatalytic activities and selectivity of CO_2 reduction on Pd-Ov-TNB, Pd-TNB and Ov-TNB are determined respectively, as shown in Fig. 7a and Table S3. CO_2 reduction products observed are CO, CH_4, C_2H_6, C_2H_4, and H_2 over different types of photocatalysts. Ov-TNB shows poor photoactivity for hydrocarbons but finds more efficient to-ward CO production with a yield of 100.27 μmol·g^{-1}·h^{-1}, suggesting that Ov act as CO_2 adsorption sites to enhance production and selectivity of CO [48]. After introducing Pd species, Pd NPs sites promote water (H_2O) dissociation to increase H* coverage and boost multiple proton-electron coupling transfer via hydrogen spillover. And thus, the proportion of hydrocarbons in CO_2 reduction products increases significantly. The yields of CH_4, C_2H_6 and C_2H_4 on sample Pd-Ov-TNB
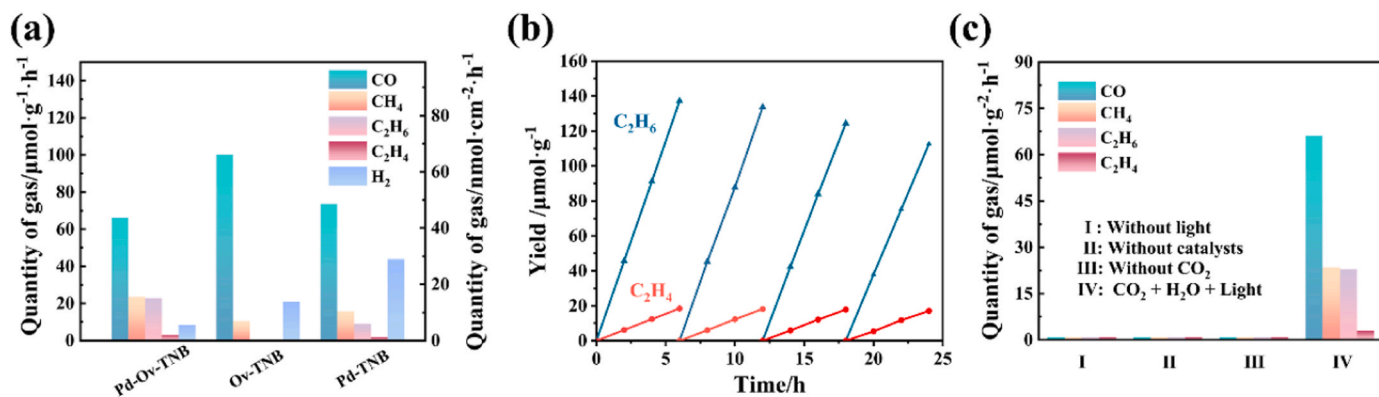
Fig. 7. (a) Gas production of photocatalytic CO_2 reduction for Pd-Ov-TNB, Ov-TNB and Pd-TNB; (b) recycling runs of Pd-Ov-TNB for photocatalytic CO_2 reduction; (c) control experiments under different conditions.

reaching 23.545 $\mu mol \cdot g^{-1} \cdot h^{-1}$, 22.9 $\mu mol \cdot g^{-1} \cdot h^{-1}$ and 3.087 $\mu mol \cdot g^{-1} \cdot h^{-1}$, respectively. Here, it is important to highlight that the Pd-Ov- TNB also yielded a large amount of valuable C_2 products with a selectivity of 51.45%, revealing great potential of the prepared catalysts for performing photocatalytic carbon-carbon coupling. A significant reduction in CO content of the product is also observed, as more CO* being hydrogenated, resulting in the formation of more abundant hydrocarbons. In contrast, the C_2 products yield of Pd-TNB is lower, with a selectivity of only 29.06%, while a higher hydrogen precipitation is observed with a yield of 43.8 $\mu mol \cdot g^{-1} \cdot h^{-1}$. The capture and activation of CO_2 by Ov are prerequisites for efficient hydrocarbons production, and the elimination of Ov leads to decrease of CO_2 reduction active sites, so more H* species binding to produce hydrogen. The elimination of ordered Ov also leads to insufficient photogenerated charge separation and therefore does not provide an electron-rich environment for hydrocarbons generation, resulting in a reduced rate of hydrocarbons generation. In addition, Mott−Schottky analysis was used to study the energy band structure of the prepared catalysts (Fig. S9b). The flat band potential of Pd-Ov-TNB, Ov-TNB and Pd-TNB are − 0.488、 − 0.427 and − 0.408 versus normal hydrogen electrode (NHE), respectively. The flat band potential of Pd-Ov-TNB appeared negative shift. The negative flat band potential is due to the increase of donor electron density and raises the Fermi level. The flat band potential (E_{fb}) for n-type semiconductors essentially coincide with their conduction band (CB) position [49]. The value of E_g and CB position can be used to obtain the corresponding band structures of samples, as shown in Fig. S9c. Notably, Pd-Ov-TNB exhibits a more negative reduction potential than other samples. From a thermodynamics stand-point, the more negative CB sites indicated that photogenerated electrons produced by Pd-Ov-TNB have strong reducing ability, which is convenient to accelerate conversion of CO_2 reaction kinetics.

To sum up, these results confirm that there are significant synergetic effects of ordered Ov and Pd decoration on enhancing CO_2RR under full-spectrum irradiation. Compared with other TiO_2-based photocatalysts reported in literatures, Pd-Ov-TNB exhibits obvious superiority, and detailed information are listed in Table S4. Furthermore, stability and reusability test of Pd-Ov-TNB for photocatalytic CO_2 reduction through cycling run is conducted. As shown in Fig. 7b, after four cyclic runs, the photoactivity of Pd-Ov-TNB does not decrease significantly, demonstrating the good stability of this photocatalyst. Moreover, XRD and SEM of the used Pd-Ov-TNB are also conducted, as shown in Figs. S10 and S11, which indicates no obvious structure and morphological variation with the fresh one, further confirming the favorable photostability of the synthesized catalysts. In addition, the control experiments of Pd-Ov-TNB sample are carried out as follows (Fig. 7c): (1) with the catalyst, CO_2, and H_2O, without light; (2) with light, CO_2, and H_2O, without the catalysts; and (3) with light, the catalyst, and H_2O, without CO_2. There is no obvious CO and hydrocarbons evolution in the control experiments,

indicating that catalysts and light are key factors for effective photocatalytic CO_2 RR.

3.4. Reaction intermediate and mechanism for CO_2 reduction

To clarify mechanism of CO_2 adsorption, activation and photoconversion in photoreduction reaction. In-situ FTIR spectroscopy analysis were performed to explore the adsorbed species and reaction intermediates on Pd-Ov-TNB and Ov-TNB photocatalysts. In-situ FTIR spectra were carried out in dark and full spectrum irradiation. As shown in Fig. 8a and b, under full spectral light irradiation, multiple characteristic peaks corresponding to adsorbed CO_2 molecules and their derived intermediates can be detected for the Pd-Ov-TNB and Ov-TNB samples. In addition to the obvious absorption peak of H_2O at 1642 cm^{-1}, monodentate carbonate (m-CO_3^{2-}, 1467–1516 cm^{-1}), bidentate carbonate (b-CO_3^{2-}, 1080 cm^{-1}), chelating-bridged carbonate (c-CO_3^{2-}, 1724 cm^{-1}), and bicarbonates species (HCO_3^-, 1199 cm^{-1}) are also observed [50–54]. These bicarbonates and carbonates are crucial indicators of CO_2 adsorption on photocatalyst surface. In particular, strong adsorption signals of CO_2 species (b-CO_2, 1562 cm^{-1}) and CO_2^- species (1687, 1247 cm^{-1}) are also detected in the target samples [55, 56]. The signals of the various peaks mentioned above indicate that the target material has active CO_2 adsorption and conversion capabilities. When light radiation is applied, the peaks of adsorbed H_2O molecules, HCO_3^- and CO_3^{2-} drop downwards rapidly, demonstrating the activation of CO_2 and the consumption and conversion of intermediates [57,58]. In addition, the bands at 1278, 1338 and 1660 cm^{-1} are from O-H deformation, C-O stretching and C=O stretching of *COOH respectively, which are thought to be crucial species driving photocatalytic CO_2 conversion process [59,60]. In particular, methoxy species (–CH_xO) at 1112 cm^{-1}, 1136 cm^{-1} and 1161 cm^{-1} are vital intermediates during CO_2 reduction to hydrocarbons. More importantly, the methyl species (–CH_3) at 1375 cm^{-1} and the ethoxy species (–CH_3CH_2O) at 1043 cm^{-1} are observed, which are the standard intermediates for C_2 products (such as ethylene and ethane) [61,62]. Interestingly, the peak intensities of these intermediate species are significantly higher on Pd-Ov-TNB than on Ov-TNB. This subtle phenomenon suggests that the high hydrocarbon selectivity of Pd-Ov-TNB might be due to the accelerated protonation of CO_2 into the abundant reaction intermediates such as –CH_xO, demonstrating the superior CO_2 conversion performance of Pd-Ov-TNB, coinciding with the above photocatalytic CO_2 reduction experimental results.

Based on the above results, we proposed the possible reaction steps of CO_2 reduction on the photocatalyst. Electron-rich Ov promote the activation of CO_2 by capturing oxygen atoms, and the adsorbed CO_2 species react with protons to form formate species (COOH*) (Eqs. (4) – (5)) [63]. The hydrogenation of CO_2 * to COOH* is a crucial step in the production of CO [64]. The formed formate species (COOH*) are usually
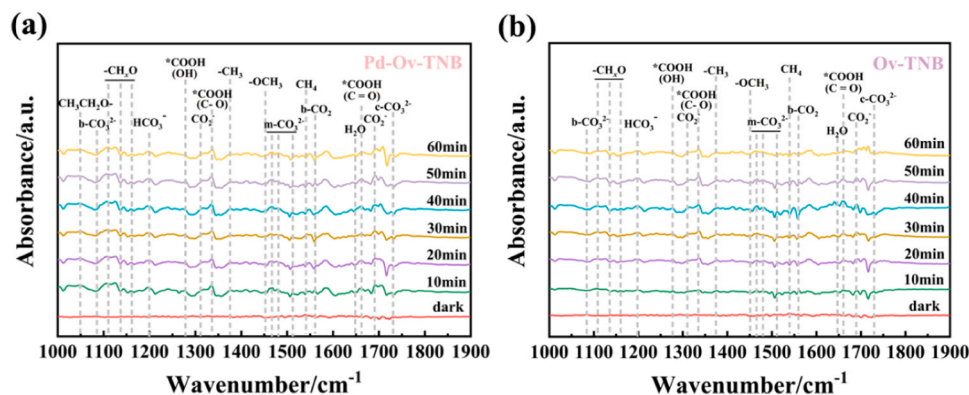
Fig. 8. In-situ DRIFTS spectra taken during photocatalytic CO_2 reduction in range of 1000–1900 cm^{-1} of (a) Pd-Ov-TNB and (b) Ov-TNB.

decomposed to formyl species (CHO*) or CO* (Eq. (6)) [65]. However, further hydrogenation of CO* to H_xCO* requires overcoming high energy barrier, so that when sufficient H* are lacking, CO* will tend to desorption to form CO (Eq. (7)) [66]. Some of the CHO* are further hydrogenated to CH_3O* intermediates and eventually to generate CH_4 (Eqs. (8)–(10)). At the metallic Pd sites, the adsorbed H_2O molecules are activated via dissociation into H atoms, which then rapidly migrate to the metal-support interface attributed to hydrogen spillover effect [67]. The abundant H* prompts the further hydrogenation of CHO* and CO* to generated OCH_2CH_3 * species [68], which is a crucial intermediate for generation of C_2 products (Eq. (11)). Finally, the OCH_2CH_3 * species can react with the H * on the support surface to generate C_2H_6 and C_2H_4 (Eqs. (12)–(13)).

$$* + CO_2 + e^- \rightarrow *CO_2^-(ads) \tag{4}$$

$$*CO_2^-(ads) + H^+ + e^- \rightarrow *COOH \tag{5}$$

$$*COOH + H^+ + e^- \rightarrow *CHO/*CO \tag{6}$$

$$*CO \rightarrow CO\uparrow \tag{7}$$

$$*CHO + H^+ + e^- \rightarrow *CH_2O \tag{8}$$

$$*CH_2O + H^+ + e^- \rightarrow *CH_3O \tag{9}$$

$$*CH_3O + 3H^+ + 3e^- \rightarrow CH_4\uparrow + H_2O \tag{10}$$

$$*CHO + *CO + 6H^+ + 6e^- \rightarrow *OCH_2CH_3 + H_2O \tag{11}$$

$$*OCH_2CH_3 + 3H^+ + 3e^- \rightarrow C_2H_6\uparrow + H_2O \tag{12}$$

$$*OCH_2CH_3 + H^+ + e^- \rightarrow C_2H_4\uparrow + H_2O \tag{13}$$
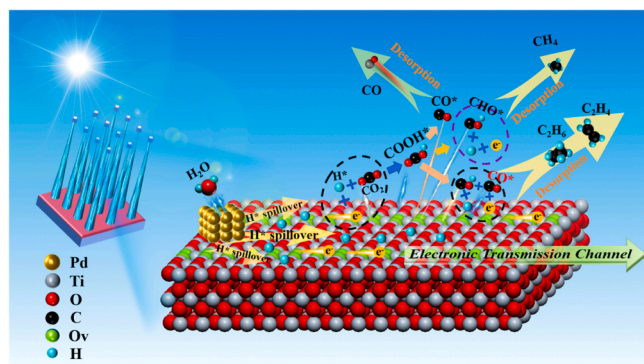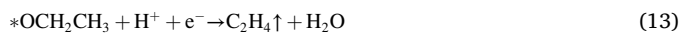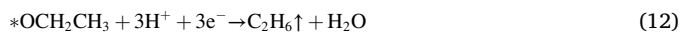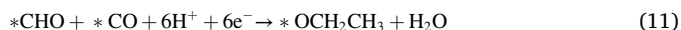

Fig. 9. The synergetic mechanism for photocatalytic conversion of CO_2 to Hydrocarbons over Pd-Ov-TNB.

On the basis of the aforementioned results and analyses, Fig. 9 illustrates the possible CO_2 reduction mechanism over Pd-Ov-TNB. Upon excitation by full solar spectrum light, the photogenerated electrons are trapped by ordered Ov and rapidly transferred to adsorbed CO_2, forming the charged species CO_2^-. Pd NPs promote the activation of adsorbed H_2O molecules by dissociation into H* , which then rapidly migrate to the metal-support interface due to the hydrogen spillover effect. The adsorbed CO_2 species react with protons to form formate species (COOH*), which are subsequently decomposed to formyl species (CHO*) and CO* . During the subsequent reaction, CO* are desorption to form CO and CHO* are further hydrogenated to CH_3O* and OCH_2CH_3 * intermediates to produce CH_4, C_2H_6 and C_2H_4. The excellent charge transfer capability of metastable ordered Ov and the hydrogen spillover effect provide an electron-rich environment and more reactive H* for the C−C coupling reaction, both of which synergistically facilitate the conversion of CO_2 to C_2 products.

4. Conclusions

In summary, TNB with metastable ordered Ov were successfully synthesized via a simple Pd-catalyzed oxygen reduction method for the selective photocatalytic conversion of CO_2 to C_2 products. During the growth of TNB, anoxic environment, appropriate temperature ranges and the internal strain in material provide the basis for Ov ordering occurs. Single crystal TNB with exposed highly active (110) facet and ordered Ov provide more active sites for CO_2 adsorption and activation, and provide an excellent architectural arrangement for accelerating charge carrier transfer. Pd NPs sites with strong electrons capture ability on the one hand boosted the dissociation of H_2O to increase H* coverage, which then rapidly migrate to the metal-support interface attributed to hydrogen spillover effect, improving the yield and selectivity of C_2 products. On the other hand, they can act as photogenerated electrons extractants to further promote photogenerated charge separation. This work provides new sight for the design of CO_2 photocatalysts, offering more opportunities for the highly selective conversion of CO_2 to C_2 products.

CRediT authorship contribution statement

Jinbo Xue: Conceptualization, Resources, Writing – review & editing. **Xin Jia:** Conceptualization, Methodology, Formal analysis, Writing – original draft. **Zhe Sun:** Software. **Huimin Li:** Formal analysis. **Qianqian Shen:** Writing – review & editing. **Xuguang Liu:** Writing – review & editing. **Husheng Jia:** Writing – review & editing. **Yongfa Zhu:** Conceptualization, Writing – review & editing.

Declaration of Competing Interest

The authors declare that they have no known competing financial

interests or personal relationships that could have appeared to influence the work reported in this paper.

Data availability

Data will be made available on request.

Acknowledgements

Appendix A. Supporting information

Supplementary data associated with this article can be found in the online version at doi:10.1016/j.apcatb.2023.123372.

References

[1] X. Liu, G. Zhang, L.W, H. Fu, Structural design strategy and active site regulation of high-efficient bifunctional oxygen reaction electrocatalysts for Zn-Air battery, Small 17 (2021), 2006766.

[2] S. Xu, E.A. C, Theoretical insights into heterogeneous (photo)electrochemical CO₂ reduction, Chem., Rev. 119 (2019) 6631–6669.

[3] J. Hu, H. Li, Q. Wu, Y. Zhao, Q. Jiao, Synthesis of TiO₂ nanowire/reduced graphene oxide nanocomposites and their photocatalytic performances, Chem. Eng. J. 263 (2015) 144–150.

[4] Z. Zou, J. Ye, K. Sayama, H. Arakawa, Direct splitting of water under visible light irradiation with an oxide semiconductor photocatalyst, Nature 414 (2001) 625–627.

[5] H. Gao, J. Wang, M. Jia, F. Yang, R.S. Andriamitantsoa, X. Huang, W. Dong, G. Wang, Construction of TiO₂ nanosheets/tetra (4-carboxyphenyl) porphyrin hybrids for efficient visible-light photoreduction of CO₂, Chem. Eng. J. 374 (2019) 684–693.

[6] A. Meng, L. Zhang, B. Cheng, J. Yu, TiO₂-MnOx-Pt hybrid multiheterojunction film photocatalyst with enhanced photocatalytic CO₂-reduction activity, ACS Appl. Mater. Interfaces 11 (2019) 5581–5589.

[7] G. Yin, X. Huang, T. Chen, W. Zhao, Q. Bi, J. Xu, Y. Han, F. Huang, Hydrogenated blue titania for efficient solar to chemical conversions: preparation, characterization, and reaction mechanism of CO₂ reduction, ACS Catal. 8 (2018) 1009–1017.

[8] L. Hao, H. Huang, Y. Zhang, T. Ma, Oxygen vacant semiconductor photocatalysts, Adv. Funct. Mater. 31 (2021), 2100919.

[9] W. Jiang, H. Loh, B.Q.L. Low, H. Zhu, J. Low, J.Z.X. Heng, K.Y. Tang, Z. Li a, X. J. Loh, E. Ye, Y. Xiong, Role of oxygen vacancy in metal oxides for photocatalytic CO₂ reduction, Appl. Catal. B Environ. 321 (2023), 122079.

[10] J. Gao, Q. Shen, R. Guan, J. Xue, X. Liu, H. Jia, Q. Li, Y. Wu, Oxygen vacancy self-doped black TiO₂ nanotube arrays by aluminothermic reduction for photocatalytic CO₂ reduction under visible light illumination, J. CO₂ Util. 35 (2020) 205–215.

[11] Y. Ji, Y. Luo, New mechanism for photocatalytic reduction of CO₂ on the anatase TiO₂(101) surface: the essential role of oxygen vacancy, J. Am. Chem. Soc. 138 (2016) 15896–15902.

[12] Y. Yan, M. Han, A. Konkin, T. Koppe, D. Wang, T. Andreu, G. Chen, U. Vetter, J. R. Morantee, P. Schaafa, Slightly hydrogenated TiO₂ with enhanced photocatalytic performance, J. Mater. Chem. A 2 (2014) 12708–12716.

[13] Y. Liu, H. Feng, X. Yan, J. Wang, H. Yang, Y. Du, W. Hao, The origin of enhanced photocatalytic activities of hydrogenated TiO₂ nanoparticles, Dalton Trans. 46 (2017) 10694–10699.

[14] J. Gao, J. Xue, S. Jia, Q. Shen, X. Zhang, H. Jia, X. Liu, Q. Li, Y. Wu, Self-doping surface oxygen vacancy-induced lattice strains for enhancing visible light-driven photocatalytic H₂ evolution over black TiO₂, ACS Appl. Mater. Interfaces 16 (2021) 18758–18771.

[15] Z. Wang, J. Zhu, X. Zu, Y. Wu, S. Shang, P. Ling, P. Qiao, C. Liu, J. Hu, Y. Pan, J. Zhu, Y. Sun, Y. Xie, Selective CO₂ Photoreduction to CH₄ via Pd^{δ+}-assisted Hydrodeoxygenation over CeO₂ Nanosheets, Angew. Chem. Int. Ed. 30 (2022), e202203249.

[16] M. Xiong, Z. Gao, Y. Qin, Spillover in heterogeneous catalysis: new insights and opportunities, ACS Catal. 5 (2021) 3159–3172.

[17] J. Li, D. Yi, F. Zhan, B. Zhou, D. Gao, D. Guo, S. Liu, X. Wang, J. Yao, Mono-layered Ru₁/TiO₂ nanosheet enables efficient visible-light-driven hydrogen evolution, Appl. Catal. B Environ. 271 (2020), 118925.

[18] L. Yuan, S. Hung, Z. Tang, H. Chen, Y. Xiong, Y. Xu, Dynamic Evolution of Atomically Dispersed Cu Species for CO₂ Photoreduction to Solar Fuels, ACS Catal. 9 (2019) 4824–4833.

[19] C. Huang, R. Guo, W. Pan, J. Tang, W. Zhou, H. Qin, X. Liu, P. Jia, Eu-doped TiO₂ nanoparticles with enhanced activity for CO₂, Photo Reduct., J. CO₂ Util. 26 (2018) 487–495.

[20] Y.L. Chueh, M. Lai, J. Liang, L. Chou, Z. Wang, Systematic Study of the Growth of Aligned Arrays of α-Fe₂O₃ and Fe₃O₄ Nanowires by a Vapor-Solid Process, Adv. Funct. Mater. 16 (2006) 2243–2251.

[21] S. Lu, B. Weng, A. Chen, X. Li, H. Huang, X. Sun, W. Feng, Y. Lei, Q. Qian, M. Yang, Facet Engineering of Pd Nanocrystals for Enhancing Photocatalytic Hydrogenation: Modulation of the Schottky Barrier Height and Enrichment of Surface Reactants, ACS Appl. Mater. Interfaces 13 (2021) 13044–13054.

[22] M. Jin, H. Liu, H. Zhang, Z. Xie, J. Liu, Y. Xia, Synthesis of Pd nanocrystals enclosed by {100} facets and with sizes <10 nm for application in CO oxidation, Nano Res 4 (2011) 83–91.

[23] A. Bai, W. Liang, G. Zheng, J. Xue, Preparation and enhanced daylight-induced photo-catalytic activity of transparent C-Doped TiO₂ thin films, J. Wuhan. Univ. Technol. Mater. Sci. Ed. 25 (2010) 738–742.

[24] Y. Yu, E. Wang, J. Yuan, Y. Cao, Enhanced photocatalytic activity of titania with unique surface indium and boron species, Appl. Surf. Sci. 273 (2013) 638–644.

[25] A. Naldoni, M. Altomare, G. Zoppellaro, N. Liu, Š. Kment, R. Zbořil, P. Schmuki, Photocatalysis with reduced TiO₂: from black TiO₂ to cocatalyst-free hydrogen production, ACS Catal. 9 (2019) 345–364.

[26] Q. Xiang, K. Lv, J. Yu, Pivotal role of fluorine in enhanced photocatalytic activity of anatase TiO₂ nanosheets with dominant (001) facets for the photocatalytic degradation of acetone in air, Appl. Catal. B Environ. 96 (2010) 557–564.

[27] S. Cai, J. Chen, Q. Li, H. Jia, Enhanced photocatalytic CO₂ reduction with photothermal effect by cooperative effect of oxygen vacancy and Au cocatalyst, ACS Appl. Mater. Interfaces 13 (2021) 14221–14229.

[28] H. Ge, B. Zhang, H. Liang, M. Zhang, K. Fang, Y. Chen, Y. Qin, Photocatalytic conversion of CO₂ into light olefins over TiO₂ nanotube confined Cu clusters with high ratio of Cu⁺, Appl. Catal. B Environ. 263 (2020), 118133.

[29] J.Y. Eom, S.J. Lim, S.M. Lee, W.H. Ryu, H. Kwon, Black titanium oxide nanoarray electrodes for high rate Li-ion microbatteries, J. Mater. Chem. A 3 (2015) 11183–11188.

[30] K. Li, B. Peng, T. Peng, Recent Advances in Heterogeneous Photocatalytic CO₂ Conversion to Solar Fuels, ACS Catal. 6 (2016) 7485–7527.

[31] S. Manivannan, S. An, J. Jeong, M. Viji, K. Kim, Hematite/M (M=Au, Pd) catalysts derived from a double-hollow Prussian blue microstructure: simultaneous catalytic reduction of o- and p- nitrophenols, ACS Appl. Mater. Interfaces 12 (2020) 17557–17570.

[32] F. Leroy, F. Borowik, Y. Cheynis, S. Almadori, M. Curiotto, J.C. Trautmann, P. Barbé, Müller, How to control solid state dewetting: A short review, Surf. Sci. Rep. 71 (2016) 391–409.

[33] T. Li, F. Hong, K. Yang, B. Yue, N. Tamura, H. Wu, Z. Cheng, C. Wang, Metastable oxygen vacancy ordering state and improved memristive behavior in TiO₂ crystals, Sci. Bull. 65 (2020) 631–639.

[34] G. Yang, G.D. Liana, E.C. Dickey, C.A. Randall, Oxygen nonstoichiometry and dielectric evolution of BaTiO₃. Part II-insulation resistance degradation under applied dc bias, J. Appl. Phys. 96 (2004) 500.

[35] A. Travlos, N. Boukos, G. Apostolopoulos, A. Dimoulas, Oxygen vacancy ordering in epitaxial layers of yttrium oxide on Si (001), Appl. Phys. Lett. 82 (2003) 4053.

[36] G.W.R. Leibbrandt, G. Hoogers, F.H.P.M. Habraken, Thin oxide film growth on Fe (100), Phys. Rev. Lett. 68 (1992) 1947.

[37] B.A. Wacaser, K.A. Dick, J. Johansson, M.T. Borgström, K. Deppert, L. Samuelson, Preferential interface nucleation: an expansion of the VLS growth mechanism for nanowires, Adv. Mater. 21 (2009) 153–165.

[38] K. Tai, K. Sun, B. Huang, S.J. Dillon, Catalyzed oxidation for nanowire growth, Nanotechnology 25 (2014), 145603.

[39] Q. Zhang, A. Gao, F. Meng, Q. Jin, S. Lin, X. Wang, D. Xiao, C. Wang, K. Jin, D. Su, E. Guo, L. Gu, Near-room temperature ferromagnetic insulating state in highly distorted LaCoO₂.₅ with CoO₅ square pyramids, Nat. Commun. 12 (2021) 1853.

[40] U. Aschauer, R. Pfenninger, S.M. Selbach, T. Grande, N.A. Spaldin, Strain-controlled oxygen vacancy formation and ordering in CaMnO₃, Phys. Rev. B. 88 (2013), 054111.

[41] T.C. Paul, J. Podder, Synthesis and characterization of Zn-incorporated TiO₂ thin films: impact of crystallite size on X-ray line broadening and bandgap tuning, Appl. Phys. A 125 (2019) 818.

[42] Z. Chen, U. Cvelbar, M. Mozetič, J. He, M.K. Sunkara, Long-range ordering of oxygen-vacancy planes in α-Fe₂O₃ nanowires and nanobelts, Chem. Mater. 20 (2008) 3224–3228.

[43] W. Che, W. Cheng, T. Yao, F. Tang, W. Liu, H. Su, Y. Huang, Q. Liu, J. Liu, F. Hu, Z. Pan, Z. Sun, S. Wei, Fast photoelectron transfer in (Cring)-C₃N₄ plane heterostructural nanosheets for overall water splitting, J. Am. Chem. Soc. 139 (2017) 3021–3026.

[44] Y. Liu, C. Miao, P. Yang, Y. He, J. Feng, D. Li, Synergetic promotional effect of oxygen vacancy-rich ultrathin TiO₂ and photochemical induced highly dispersed Pt for photoreduction of CO₂ with H₂O, Appl. Catal. B Environ. 244 (2019) 919–930.

[45] D. Jiang, Y. Zhou, Q. Zhang, Q. Song, C. Zhou, X. Shi, D. Li, Synergistic Integration of AuCu Co-Catalyst with Oxygen Vacancies on TiO₂ for Efficient Photocatalytic Conversion of CO₂ to CH₄, ACS Appl. Mater. Interfaces 13 (2021) 46772–46782.

[46] X. Li, S. Fang, L. Ge, C. Han, P. Qiu, W. Liu, Synthesis of flower-like Ag/AgCl-Bi$_2$MoO$_6$ plasmonic photocatalysts with enhanced visible-light photocatalytic performance, Appl. Catal. B Environ. 176 177 (2015) 62–69.

[47] J. Liu, F. Wang, X. Chen, R. Li, P. Yan, S. Bai, X. Yang, J. Zhang, Unraveling the lattice matching effect in surface phase junctions for interfacial charge separation, J. Phys. Chem. C. 125 (2021) 14188–14194.

[48] W. Chen, X. Liu, B. Han, S. Liang, H. Deng, Z. Lin, Boosted photoreduction of diluted CO$_2$ through oxygen vacancy engineering in NiO nanoplatelets, Nano Res 14 (2021) 730–737.

[49] M. Tahir, N.S. Amin, Indium-doped TiO$_2$ nanoparticles for photocatalytic CO$_2$ reduction with H$_2$O vapors to CH$_4$, Appl. Catal. B Environ. 162 (2015) 98–109.

[50] P. Tian, G. Zhan, J. Tian, K.B. Tan, M. Guo, Y. Han, T. Fu, J. Huang, Q. Li, Direct CO$_2$ hydrogenation to light olefins over ZnZrOx mixed with hierarchically hollow SAPO-34 with rice husk as green silicon source and template, Appl. Catal. B Environ. 315 (2022), 121572.

[51] J. Sheng, Y. He, J. Li, C. Yuan, H. Huang, S. Wang, Y. Sun, Z. Wang, F. Dong, Identification of halogen-associated active sites on bismuth-based perovskite quantum dots for efficient and selective CO$_2$-to-CO photoreduction, ACS Nano 14 (2020) 13103–13114.

[52] Y. Cao, L. Guo, M. Dan, D.E. Doronkin, C. Han, Z. Rao, Y. Liu, J. Meng, Z. Huang, K. Zheng, P. Chen, F. Dong, Y. Zhou, Modulating electron density of vacancy site by single Au atom for effective CO$_2$ photoreduction, Nat. Commun. 12 (2021) 1675.

[53] J. Sheng, Y. He, M. Huang, C. Yuan, S. Wang, F. Dong, Frustrated lewis pair sites boosting CO$_2$ photoreduction on Cs$_2$CuBr$_4$ perovskite quantum dots, ACS Catal. 12 (2022) 2915–2926.

[54] H. Shang, X. Wang, H. Li, M. Li, C. Mao, P. Xing, S. Zhao, Z. Chen, J. Sun, Z. Ai, L. Zhang, Oxygen vacancies promote sulfur species accumulation on TiO$_2$ mineral particles, Appl. Catal. B Environ. 290 (2021), 120024.

[55] K. Tang, Z. Wang, W. Zou, H. Guo, Y. Wu, Y. Pu, Q. Tong, H. Wan, X. Gu, L. Dong, J. Rong, Y. Chen, Advantageous role of Ir^0 supported on TiO$_2$ nanosheets in photocatalytic CO$_2$ reduction to CH$_4$: fast electron transfer and rich surface hydroxyl groups, ACS Appl. Mater. Interfaces 13 (2021) 6219–6228.

[56] W. Su, J. Zhang, Z. Feng, T. Chen, P. Ying, C. Li, Surface phases of TiO$_2$ nanoparticles studied by UV raman spectroscopy and FT-IR spectroscopy, J. Phys. Chem. C. 112 (2008) 7710–7716.

[57] J. Zhu, W. Shao, X. Li, X. Jiao, J. Zhu, Y. Sun, Y. Xie, Asymmetric triple-atom sites confined in ternary oxide enabling selective CO$_2$ photothermal reduction to acetate, J. Am. Chem. Soc. 143 (2021) 18233–18241.

[58] K. Wang, J. Lu, Y. Lu, C.H. Lau, Y. Zheng, X. Fan, Unravelling the C -C coupling in CO$_2$ photocatalytic reduction with H$_2$O on Au/TiO$_{2-x}$: combination of plasmonic excitation and oxygen vacancy, Appl. Catal. B Environ. 292 (2021), 120147.

[59] J. Yi, R. Xie, Z. Xie, G. Chai, T. Liu, R. Chen, Y. Huang, R. Cao, Highly Selective CO$_2$ Electroreduction to CH$_4$ by In Situ Generated Cu$_2$O Single-Type Sites on a Conductive MOF: Stabilizing Key Intermediates with Hydrogen Bonding, Angew. Chem. Int. Ed. 59 (2020) 23641–23648.

[60] T. Zheng, K. Jiang, N. Ta, Y. Hu, J. Zeng, J. Liu, H. Wang, Highly Selective Two-Electron Electrocatalytic CO$_2$ Reduction on Single-Atom Cu, Catal., Joule 3 (2019) 265–278.

[61] X. Li, W. He, C. Li, B. Song, S. Liu, Synergetic surface modulation of ZnO/Pt@ZIF-8 hybrid nanorods for enhanced photocatalytic CO$_2$ valorization, Appl. Catal. B Environ. 287 (2021), 119934.

[62] W. Jiang, J. Low, K. Mao, D. Duan, S. Chen, W. Liu, C. Pao, J. Ma, S. Sang, C. Shu, X. Zhan, Z. Qi, H. Zhang, Z. Liu, X. Wu, R. Long, L. Song, Y. Xiong, Pd-modified ZnO-Au enabling alkoxy intermediates formation and dehydrogenation for photocatalytic conversion of methane to ethylene, J. Am. Chem. Soc. 143 (2021) 269–278.

[63] J. Fu, K. Jiang, X. Qiu, J. Yu, M. Liu, Product selectivity of photocatalytic CO$_2$ reduction reactions, Mater. Today 32 (2020) 222–243.

[64] W. Bi, Y. Hu, N. Jiang, L. Zhang, H. Jiang, X. Zhao, C. Wang, C. Li, Ultra-fast construction of plaque-like Li$_2$TiO$_3$/TiO$_2$ heterostructure for efficient gas-solid phase CO$_2$ photoreduction, Appl. Catal. B Environ. 269 (2020), 118810.

[65] F. He, J. Zhuang, B. Lu, X. Liu, J. Zhang, F. Gu, M. Zhu, J. Xu, Z. Zhong, G. Xu, F. Su, Ni-based catalysts derived from Ni-Zr-Al ternary hydrotalcites show outstanding catalytic properties for low-temperature CO$_2$ methanation, Appl. Catal. B Environ. 293 (2021), 120218.

[66] X. Wang, Z. Wang, Y. Li, J. Wang, G. Zhang, Efficient photocatalytic CO$_2$ conversion over 2D/2D Ni-doped CsPbBr$_3$/Bi$_3$O$_4$ Br Z-scheme heterojunction: Critical role of Ni doping, boosted charge separation and mechanism study, Appl. Catal. B Environ. 319 (2022), 121895.

[67] P. Hongmanorom, J. Ashok, P. Chirawatkul, S. Kawi, Interfacial synergistic catalysis over Ni nanoparticles encapsulated in mesoporous ceria for CO$_2$ methanation, Appl. Catal. B Environ. 297 (2021), 120454.

[68] B. Ni, H. Jiang, W. Guo, Q. Xu, Y. Min, Tailoring the oxidation state of metallic TiO through Ti^{3+}/Ti^{2+} regulation for photocatalytic conversion of CO$_2$ to C$_2$H$_6$, Appl. Catal. B Environ. 307 (2022), 121141.